

Multiscale modeling of electroosmotic flow: Effects of discrete ion, enhanced viscosity, and surface friction

Ravi Bhaduria and N. R. Aluru^{a)}

Department of Mechanical Science and Engineering, Beckman Institute for Advanced Science and Technology, University of Illinois at Urbana-Champaign, Urbana, Illinois 61801, USA

(Received 20 February 2017; accepted 18 April 2017; published online 10 May 2017)

We propose an isothermal, one-dimensional, electroosmotic flow model for slit-shaped nanochannels. Nanoscale confinement effects are embedded into the transport model by incorporating the spatially varying solvent and ion concentration profiles that correspond to the electrochemical potential of mean force. The local viscosity is dependent on the solvent local density and is modeled using the local average density method. Excess contributions to the local viscosity are included using the Onsager-Fuoss expression that is dependent on the local ionic strength. A Dirichlet-type boundary condition is provided in the form of the slip velocity that is dependent on the macroscopic interfacial friction. This solvent-surface specific interfacial friction is estimated using a dynamical generalized Langevin equation based framework. The electroosmotic flow of Na^+ and Cl^- as single counterions and NaCl salt solvated in Extended Simple Point Charge (SPC/E) water confined between graphene and silicon slit-shaped nanochannels are considered as examples. The proposed model yields a good quantitative agreement with the solvent velocity profiles obtained from the non-equilibrium molecular dynamics simulations. *Published by AIP Publishing.* [<http://dx.doi.org/10.1063/1.4982731>]

I. INTRODUCTION

Electroosmotic flow (EOF) is a type of electrokinetic phenomenon observed in electrolytic solutions where the solvent is set into motion under the influence of an applied potential gradient or electric field. The coupled electro-hydrodynamic motion of solvent and ions is commonly observed in the presence of the charged solid-liquid interface in naturally occurring substances such as silica and clay,^{1,2} as well as in complex biological systems like DNA and transmembrane protein channels such as α -hemolysin.³ The practical need to study EOF arises from the necessity to control and manipulate the flow rates for a wide array of engineering systems such as proton exchange membranes in fuel cells,⁴ micro/nano-scale pumps and lab-on-a-chip devices, separation science and energy conversion,^{5,6} power generation,⁷ and artificial pores for water purification.⁸ These complex systems operate at small length scales where the surface effects are particularly dominant. Therefore, a deeper physical understanding of the electro-hydrodynamic motion at the nanoscale is warranted.

The presence of a charged wall at the solid-liquid interface results in ionic charge accumulation, thereby breaking the local electro-neutrality (although the global electro-neutrality is always preserved). In a pore/channel like geometry, the accumulated charge concentration decreases from an enhanced value near the wall to a lower value in the center of the channel, resulting in the formation of the electrical double layer (EDL).^{9,10} The EDL is rich in the charge opposite to that of the wall (counter-ions) and has been classically theorized as that comprised of an immobile Stern layer that consists of

counter-ions adsorbed on the wall due to their electrostatic interactions,¹¹ and a mobile diffuse layer that is capable of transferring momentum to the solvent. When an electric field tangential to the wall is applied, the transfer of momentum from ions to the solvent occurs via the ion/solvent friction forces. Although the ion to solvent momentum transfer is primarily manifested in the EDL, the tangential momentum is transferred away from the wall via the action of viscous stresses in the solvent.¹⁰

The classical treatment of EOF formulates the charge distribution in the pore using the Gouy-Chapman (GC) theory that is based on the Poisson-Boltzmann (PB) equation. The GC theory provides the theoretical measure of the driving force in the Navier-Stokes (NS) equations. The GC theory, being a mean-field approach, predicts a charge distribution that is exponential in nature and is, therefore, unrealistic as it fails to account for the finite size of the ions.¹² Although the steric effects have been modeled successfully by Stern¹¹ and later in a modified PB model proposed by Bikerman,¹³ the PB equation based models still neglect the effects of solvent polarization due to the treatment of the solvent permittivity as a constant value. The Langevin-Bikerman model rectifies the shortcomings of the previous models by including the effects of finite size and solvent polarization.¹⁴ A comprehensive model for EOF should account for correct charge distribution that incorporates electrochemical potential of mean force (PMF) on the ions,¹⁵ along with appropriate space dependent solvent polarization.¹⁶

In addition to the approximations involved in predicting the correct charge distribution and the resultant driving force for EOF, the assumption of solvent viscosity being equal to its pure component value (in the absence of ions and charged wall) introduces significant deviations from non-equilibrium

^{a)}Electronic mail: aluru@illinois.edu

molecular dynamics (NEMD) calculations of EOF.¹⁵ The viscosity of the solvent is enhanced in the EDL due to the presence of a charged surface and the ions.¹⁷ This interfacial thickening of the solvent has been systematically studied for EOF driven by monovalent counter-ions of similar size by inverting the NEMD velocity profiles.¹⁸ Here, the positively charged wall demonstrated a higher degree of solvent viscosity enhancement compared to the negatively charged wall with equal magnitude of surface charge density. The resultant NEMD velocity profiles in the positively and negatively charged pores also exhibited significant differences. The reason for the viscosity enhancement has been theorized as the increase in the hydrogen bonding of water near the positively charged surface¹⁹ and is also shown to be dependent on the magnitude of the surface charge density.²⁰

The presence of the charged surface also modulates the effective interfacial friction experienced by the solvent and ions, thereby affecting their slippage near the wall. Joly *et al.*²¹ have performed MD simulations of ions in a spherically symmetric solvent and have provided expressions for the interfacial friction coefficient and slip length. These expressions exhibit dependence on the wall surface charge density and implicit dependence on the solvent permittivity through the characteristic parameter Bjerrum length. However, the force correlation that appears in their computation of the solvent friction also contains contributions from ion-wall interactions. Also, the assumption of a non-polar solvent does not account for realistic ion-solvent electrostatic interactions. To provide the measure of ion-wall friction separately, Netz considered the ion-wall interaction mediated by an implicit solvent, which demonstrates a reduction in ionic mobilities in the interfacial region.²² The contact-adsorption of ions at the wall has also been linked to the increase in the solvent viscosity.²³

In our previous work,^{24,25} we have characterized the slip of a single component fluid and binary mixtures using a multiscale, phenomenological Generalized Langevin Equation (GLE) based slip model. In these friction based models, we evolve the trajectories of the interfacial particles using GLE, while also accounting for the total PMF of the fluid. The thermal noise characteristics of the confined fluid are considered to be the same as in its bulk like state. From this dynamical framework, a macroscopic friction parameter is computed using the wall-fluid structure force autocorrelation function (FACF) and wall-fluid force-velocity cross correlation function (FVCCF),²⁶ which is subsequently utilized in a one-dimensional (1D) continuum transport model as a boundary condition. We also demonstrated the equivalence between the friction based Robin boundary condition (FBC) and Dirichlet condition relating the slip velocity to the friction coefficient.

In this work, we extend our multiscale transport model for EOF. The relevant equation of momentum for the solvent accounts for the spatial variation of ion concentration and solvent viscosity. The enhancement in the solvent viscosity is embedded using the Onsager-Fuoss type expression²⁷ over the pure component viscosity profile predicted using the Local Average Density Method (LADM).²⁸⁻³⁰ The form of the

Onsager-Fuoss expression includes the effects from variations in solvent permittivity, ionic strength, and ion conductivities. The boundary conditions are provided in terms of the slip velocity, which in turn depends upon the macroscopic interfacial friction parameter. The estimate of solvent interfacial friction is separately obtained using the GLE framework. The remainder of the paper is organized as follows: in Sec. II we present the relevant 1D EOF transport model. In Sec. III, we discuss the model for viscosity enhancement, while the GLE based friction model is presented in Sec. IV. In Sec. V, we provide brief details on the MD and GLE simulations. In Sec. VI, we discuss the results obtained from the EOF model and compare them with NEMD. Finally, we draw conclusions in Sec. VII.

II. TRANSPORT MODEL

The relevant 1D formulation for an isothermal, low Reynolds number, electroosmotic flow in a slit channel can be written as a Stokes equation^{18,19}

$$\frac{d}{dz} \left[\mu(z) \frac{du_{eo}}{dz} \right] + \sum_{i \in \pm} \rho_i(z) \tilde{z}_i e E_x^{\text{ext}} = 0, \quad (1)$$

with boundary conditions

$$u_{eo} \left(-\frac{L}{2} + \delta \right) = u_{eo} \left(+\frac{L}{2} - \delta \right) = u_s, \quad (2)$$

where L is the channel width, with confining walls located at $\pm L/2$, and (x, z) are the streaming and confined directions, respectively. $u_{eo}(z)$ is the EOF velocity field in the streaming direction, e is the electronic charge, E_x^{ext} is the applied electric field in the direction parallel to the wall, $\rho_i(z)$ is the ion concentration field, and \tilde{z}_i is the valency of the ion i , which may be a cation (+) or anion (-). The summation runs over all ionic species ($i \in \pm$) to compute the total electroosmotic driving force. Spatial variation of the solvent viscosity $\mu(z)$ is considered to reflect its dependence on inhomogeneous properties along the confined direction such as solvent and ion densities, solvent permittivity, and ion conductivity. Dirichlet type boundary conditions are provided at a distance δ from the wall, which is the first location where the solvent density (ρ_0) satisfies $\rho_0 > \rho_{0,\text{tol}}$, with u_s as the electroosmotic slip velocity. The boundary conditions are expressed in the FBC form as

$$A \mu(z) \frac{du_{eo}(z)}{dz} \Big|_{z=-L/2+\delta} = \zeta_0 u_s, \quad (3)$$

where A is the interfacial area and ζ_0 is a macroscopic parameter known as the interfacial friction coefficient of the solvent. In addition, a symmetry boundary condition at the center point of the channel can be written as

$$\frac{du_{eo}(z)}{dz} \Big|_{z=0} = 0. \quad (4)$$

As discussed previously,²⁴ we can recast Eqs. (1), (3), and (4) to provide an expression for the electroosmotic slip velocity as

$$u_s = \frac{AeE_x^{\text{ext}}}{\zeta_0} \sum_{i \in \pm} \tilde{z}_i \int_{-L/2}^0 \rho_i(z) dz. \quad (5)$$

This value of the electroosmotic slip velocity is used as a boundary condition in Eq. (2). Inputs required for this framework are the ion concentration, solvent viscosity, and the interfacial friction coefficient for the solvent. The methods to obtain these inputs are discussed below.

III. ION CONCENTRATION AND SOLVENT VISCOSITY VARIATION

In this section, we discuss methodologies to capture inhomogeneities of the fluid properties in the confined direction. Due to the presence of charged confining walls, the electrochemical PMF of ions and the polar solvent (SPC/E water in our case) shows oscillations normal to the wall. Consequently, the density profiles exhibit significant layering in the confined direction. Variations in the ion/solvent densities can be quantified using MD simulations with appropriate spatial binning. Alternatively, one can utilize continuum based theories such as the recently proposed empirical potential based quasi-continuum theory (EQT),^{31–38} which a multiscale formulation to compute the density and the corresponding PMF profiles in the nanochannel. The advantages of using EQT over particle-based methods are significant in terms of computing speed since it is orders of magnitude faster. Recently, the approach has also been used to calculate various thermodynamic properties in confined systems, e.g., lateral and confined direction pressure, surface tension, solvation force, and adsorption isotherms.³⁶ The EQT framework has also been extended to study multicomponent systems, such as a binary Lennard-Jones (LJ) mixture,³⁷ and ion/solvent systems with charged walls.³⁸ Since our objective in this work is to calculate the EOF velocity profiles, we have used the density and PMF profiles obtained from EMD simulations.

Due to the inhomogeneities of the solvent density and the presence of mobile ions and charged walls, solvent viscosity is not a constant value; instead it varies along the confinement. The total viscosity variation due to both of these effects can be apportioned separately as

$$\mu(z) = \mu_p(z) + \mu_{ex}(z), \quad (6)$$

where $\mu_p(z)$ is the pure-component viscosity profile, and it only models the effects of solvent density variation on the total viscosity, while $\mu_{ex}(z)$ is the variation of the excess part of the viscosity due to the presence of charges (ions and charged walls). We use the LADM^{28–30} to predict the pure-component viscosity profile. Here, the 1D solvent density profile $\rho_0(z)$ is first weight-averaged to obtain a coarse-grained density profile as

$$\bar{\rho}_0(z) = \frac{6}{\sigma_0^3} \int_{|z-z'| < \sigma_0/2} \left[\left(\frac{\sigma_0}{2} \right)^2 - (z-z')^2 \right] \rho_0(z') dz', \quad (7)$$

where the average is performed over the length scale of the solvent LJ diameter σ_0 . The coarse grained solvent density $\bar{\rho}_0$ along with temperature T provides an equivalent homogeneous, pure-component thermodynamic state of the solvent, which can then be utilized to compute the local pure-component viscosity $\mu_p(z)$ using an appropriate equation of state.²⁴

The corresponding change in the excess viscosity $\mu_{ex}(z)$ of the solvent is dependent on the concentration of the ions. The preliminary estimates of the excess term were provided by Falkenhagen,³⁹ which are valid for symmetrical electrolytes, and later extended by Onsager and Fuoss²⁷ to account for asymmetrical electrolytes. It is noteworthy that both of these expressions were obtained using the Debye-Hückel theory. More rigorous, microscopic expressions for the excess viscosity have also been derived by Chandra and Bagchi,⁴⁰ where they have used the mode coupling theory (MCT) to account for the realistic ion-ion transverse stress correlations. Their expression also reduces to that of Falkenhagen in the limit of low ionic concentration. However, their formulation involves the computation of additional parameters such as ionic structure factors and the frequency dependent van Hove functions. In this work, we use the Onsager-Fuoss excess viscosity model, where the working equations are summarized as

$$\mu_{ex}(z) \approx a \left(\frac{2I(z)}{\epsilon_r(z)T} \right)^{1/2} \sum_{i \in \pm} \frac{\psi_i(z) |\bar{z}_i|}{\lambda_i(z)}, \quad (8)$$

where the ionic strength $I(z) = 0.5 \sum_{i \in \pm} \rho_i(z) \bar{z}_i^2$ and $\psi_i(z) = \rho_i(z) \bar{z}_i^2 / 2I(z)$. The relative permittivity of solvent ϵ_r and ion conductivities λ_i are considered to be inhomogeneous in the confinement, and T is the operating temperature. The constant a is defined as

$$a = \frac{F e^2 10^8}{480\pi} \left(\frac{10^{-3} N_A}{\epsilon_0 k_B} \right)^{1/2} = 0.36452678, \quad (9)$$

where F is Faraday's constant, ϵ_0 is the permittivity of vacuum, k_B is the Boltzmann constant, and N_A is Avogadro's constant. The expression of a provides the value of viscosity in SI units (Pa-s) when ion densities and ionic strength are expressed in molar concentration units (mol/l or M) and ionic conductivities are expressed in $\Omega^{-1} \text{ mol}^{-1} \text{ cm}^2$.

To capture the spatial variation of relative permittivity of solvent (ϵ_r), we utilize the polarization model^{14,38,41} as

$$\epsilon_r(z) = 1 - \frac{P(z)}{\epsilon_0 \phi'(z)}, \quad (10)$$

where ϵ_0 is the vacuum permittivity, $P(z)$ is the variation of solvent polarization, $\phi(z)$ is the electrostatic potential, and $\phi'(z) = d\phi/dz$. The solvent polarization is calculated as

$$P(z) = \rho_0(z) \mu_d \langle \cos \theta(z) \rangle, \quad (11)$$

where μ_d is the magnitude of the solvent dipole moment and $\langle \cos \theta(z) \rangle$ is the mean cosine of the angle of the solvent dipole vector with the z -axis. Its variation in the confinement is calculated using the Langevin point dipole model as¹⁴

$$\langle \cos \theta(z) \rangle = -\mathcal{L}(\beta \mu_d \phi'(z)), \quad (12)$$

where $\mathcal{L} = (\coth(x) - 1/x)$ is the Langevin function and $\beta = 1/k_B T$. To calculate the electrostatic potential $\phi(z)$, we solve a 1D Poisson equation

$$\frac{d}{dz} \left(\epsilon_r(z) \frac{d\phi}{dz} \right) = -\frac{1}{\epsilon_0} \sum_{i \in \pm} \rho_i(z) \bar{z}_i e, \quad (13)$$

with boundary conditions

$$\left. \frac{d\phi}{dz} \right|_{z=\pm L/2} = \pm \frac{\sigma_{\text{wall}}}{\epsilon_0}, \quad (14a)$$

$$\phi(z=0) = 0, \quad (14b)$$

where σ_{wall} is the wall-charge density. Ion concentration values from the EMD simulation are used to solve the Poisson equation. Eqs. (10)–(13) are solved self-consistently to obtain the variation of the relative permittivity $\epsilon_r(z)$, polarization $P(z)$, average dipole angle $\langle \cos \theta(z) \rangle$, and 1D electrostatic potential $\phi(z)$. Here, the value of the solvent dipole moment is calculated by taking the limit $\phi'(z) \rightarrow 0$ in Eq. (10) as

$$\epsilon_{r,b} = 1 + \frac{\rho_{0,b} \mu_d^2 \beta}{3\epsilon_0}, \quad (15)$$

where $\epsilon_{r,b}$ is the bulk value of relative permittivity of the solvent (in the absence of an external electric field) and $\rho_{0,b}$ is the bulk density of the solvent. Further details on the polarization model are presented in Refs. 14, 38, and 41.

For calculating the ionic conductivity, the following equations are utilized:⁴²

$$\lambda_i(z) = \left(\frac{F^2}{RT} \right) D_i^0 \gamma_i^{\alpha_i}, \quad (16a)$$

$$\log_{10} \gamma_i(z) = -\tilde{A} z_i^2 \sqrt{I(z)}, \quad (16b)$$

where $\tilde{A} = 0.5085 \text{ M}^{-1/2}$ is a constant, $R = k_B N_A$ is the universal gas constant, and D_i^0 is the ion diffusivity in the solvent at infinite dilution, i.e., in the limit $\rho_{\pm} \rightarrow 0$. At infinite dilution limit, the activity coefficient $\gamma_i \rightarrow 1$ and Eq. (16a) reduces to the Nernst-Einstein equation. For finite densities, an ion-ion correlation based correction factor is introduced via the parameter α_i that is parameterized as⁴³

$$\alpha_i(z) = \begin{cases} 0.6/|\tilde{z}_i|^{0.5}, & \text{if } I(z) < 0.36 \text{ M}, \\ \sqrt{I(z)}/|\tilde{z}_i|, & \text{otherwise.} \end{cases} \quad (17)$$

At this stage, all inhomogeneous confinement effects have been included in the model. In Sec. IV, we discuss the GLE based friction model for electroosmotic slip.

IV. SOLVENT INTERFACIAL FRICTION DUE TO CHARGED WALL: BOUNDARY CONDITIONS

In this section, we present the methodology to estimate the friction ζ_0 between a charged wall and a polar solvent. We begin with the analysis first presented by Huang and Szlufarska²⁶ that was later adapted for SPC/E water near an uncharged wall²⁴ and binary mixtures.²⁵ The friction contribution ζ_0^j from a single solvent particle j in the interfacial region can be expressed as

$$\zeta_0^j = \frac{\int_0^{\infty} \langle f_{x,j}^{\text{wf}}(0) f_{x,j}^{\text{wf}}(t) \rangle dt}{k_B T + \int_0^{\infty} \langle v_{x,j}(0) v_{x,j}^{\text{wf}}(t) \rangle dt}, \quad (18)$$

where $f_{x,j}^{\text{wf}}$ and $v_{x,j}$ are the instantaneous streaming direction wall-solvent force and velocity of the solvent particle near the solid wall, respectively. The time correlation appearing in the numerator is the wall-solvent FACF, while the denominator contains wall-solvent FVCCF. The angular brackets $\langle \cdot \rangle$ denote the ensemble average of the quantities. Exploiting the additive nature of the friction, the total value of the macroscopic

friction coefficient is obtained by adding the contributions from all interfacial solvent particles as $\zeta_0 = \sum_j \zeta_0^j$. This value of solvent friction is further used to calculate the EOF slip velocity described by Eq. (5), resulting in the closure of the EOF model.

The trajectory of the representative solvent particle j is generated using the coarse-grained phenomenological dynamical framework of GLE.^{24,25} The relevant equations of motion of the representative particle include a dissipative, non-Markovian friction force and its corresponding random force that is orthogonal to the particle velocity, as explained in the Mori-Zwanzig projection operator formalism.^{44–46} The equations of motion can be written as

$$m_0 \frac{dv_{z,j}(t)}{dt} = -m_0 \int_0^t K_0(t-t') v_{z,j}(t') dt' + f_{z,j}^{\text{tot}}(t) + R_{z,j}(t), \quad (19a)$$

$$m_0 \frac{dv_{x,j}(t)}{dt} = -m_0 \int_0^t K_0(t-t') v_{x,j}(t') dt' + f_{x,j}^{\text{tot}}(t) + R_{x,j}(t), \quad (19b)$$

$$\frac{dz_j(t)}{dt} = v_{z,j}(t), \quad \frac{dx_j(t)}{dt} = v_{x,j}(t), \quad (19c)$$

where m_0 is the mass of the particle j representing the solvent molecule, $v_{z,j}$ and $v_{x,j}$ are its instantaneous velocities, and $f_{z,j}$ and $f_{x,j}$ are the structure based forces acting on the particle in the confined and the streaming directions, respectively. The random forces $R_{z,j}(t)$ and $R_{x,j}(t)$ in the corresponding directions have zero mean, i.e., $\langle R_{x/z,j}(t) \rangle = 0$, and they follow the fluctuation-dissipation theorem as $\langle R_{x/z,j}(0) R_{z/j}(t) \rangle = m_0 k_B T K_0(t) \delta_{xz}$, with δ_{xz} being the Kronecker delta. In addition to that, being orthogonal to the velocity,⁴⁶ they also satisfy $\langle v_{x/z,j}(0) R_{x/z,j}(t) \rangle = 0$. The memory function of the solvent $K_0(t)$ is assumed to be isotropic and therefore ensures the identical statistical properties of the thermal noise in both streaming and confined directions. The memory function is assumed to be same as that of the bulk water at a density of 33.46 molecules/nm³ and has been reported in tabular form as supplementary information in our previous work.²⁴

The structure based instantaneous force values on the particle are sampled using the static mean force maps as $f_{z,j}^{\text{tot}}(t) = F_z^{\text{tot}}(z_j(t))$ and $f_{x,j}^{\text{tot}}(t) = F_x^{\text{tot}}(x_j(t), z_j(t))$. It has been demonstrated earlier by Sanghi and Aluru⁴⁷ that the GLE formulation in Eq. (19a) is sufficient in accurately describing the dynamics of the representative particle in the confined direction. In their work, the 1D variation of structure based force is calculated as $F_z^{\text{tot}}(z) = -dU_{\text{1D}}^{\text{tot}}(z)/dz$, where $U_{\text{1D}}^{\text{tot}}(z)$ is the 1D variation of the solvent total PMF. The total PMF, in turn, can be evaluated from the density profile of solvent as $U_{\text{1D}}^{\text{tot}}(z) = -k_B T \log(\rho_0(z)/\rho_{0,b})$, where $\rho_{0,b}$ is the density of the solvent in the bulk like center region of the confinement.

The streamwise force map ($F_x^{\text{tot}}(x, z)$) is periodic in the x -direction, reflecting the lattice structure of the wall on the solvent. Additionally, its amplitude decays in the z -direction

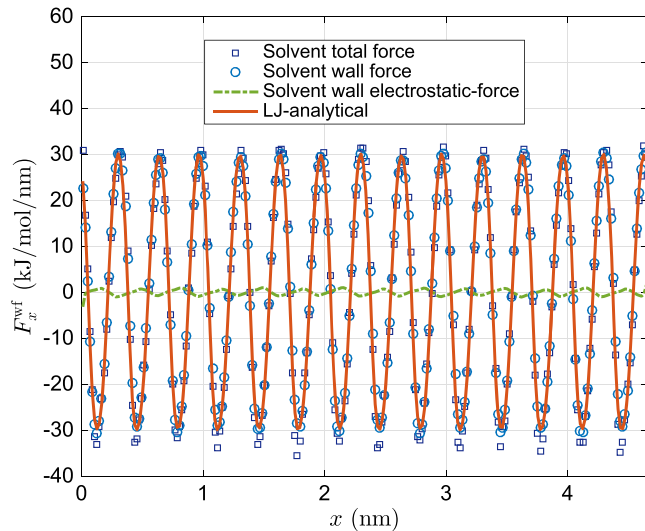


FIG. 1. Comparison of solvent streamwise forces for NaCl and the SPC/E water system confined in silicon walls. Total force (squares) contains contributions from ion-solvent, solvent-solvent, and wall-solvent interactions. Wall-solvent (circles) include LJ and electrostatic (green dashed-dotted line) contributions. Also plotted is the analytical LJ force map (red solid line) computed using the method discussed in Ref. 24.

and becomes zero beyond the interfacial region as the solvent is homogenized. Therefore, 2D maps of $F_x^{\text{tot}}(x, z)$ and $F_x^{\text{wf}}(x, z)$ are required to capture the effects of lattice structure on the solvent friction coefficient. We compare the force maps computed using the EMD simulations, at the location of the solvent density peak, for NaCl and the SPC/E water system confined between silicon walls, in Fig. 1. It can be noted that near the interface, the wall-solvent forces are dominant and they approximate the total forces on the solvent as $F_x^{\text{tot}}(x, z) \approx F_x^{\text{wf}}(x, z)$. Further, the wall-solvent electrostatic contribution to the streamwise forces is also found to be negligible. Based on these observations, one can deduce that the wall-solvent LJ forces are the pertinent forces for simulating the GLE based interfacial dynamics. Their 2D map can be analytically computed as discussed in Ref. 24 and is used to solve the streamwise direction GLE (Eq. (19b)). Details to solve the GLE framework are provided in Sec. V, and the accuracy of the correlations computed using the GLE framework with respect to the EMD simulations is discussed in Sec. VI.

V. SIMULATION DETAILS

We perform different types of MD simulations in the present work using the LAMMPS package.⁴⁸ Water is modeled using the SPC/E model.⁴⁹ Ions are considered as monovalent ($\bar{z}_{\pm} = \pm 1$) and modeled as 12-6 LJ spheres with point charges at their center. LJ interaction parameters for unlike particles are estimated using the Lorentz-Berthelot combination rules and are truncated at 1.4 nm. In this work, we consider sodium and chloride ions as cation and anion, respectively, with the ion-water force-field parameters provided by Smith and Dang,⁵⁰ which have yielded good estimates of transport properties such as viscosity.⁵¹ Water and graphene carbon interactions are modeled using the force field of Gordillo and

TABLE I. LJ interaction parameters in MD simulations.

Atom	σ (nm)	ϵ (kJ/mol)
H	0.0	0.0
O	0.317	0.6503
Na ⁺	0.235	0.5439
Cl ⁻	0.44	0.4184
C	0.339	0.2334
Si	0.3385	2.447

Marti.⁵² A summary of the simulation force field parameters is provided in Table I. First, bulk EMD simulations of single ions in water are performed to calculate the limiting value of ionic diffusivity. Here, only short-range electrostatic interactions are considered using a cutoff value of 0.9 nm, to avoid the interaction of the ion with its periodic image. The exclusion of long-range electrostatics for single ion in bulk water EMD simulations does not introduce significant errors in computation of ionic diffusivities.^{53,54} The limiting ionic diffusion coefficient is computed using the integral of the velocity autocorrelation function (VACF) of the ion and is further used to calculate the ionic conductivity in Eq. (16a).

In this work, we consider six examples of EOF in semi-infinite slit channels made up of two different surfaces that highlight the contrasting level of friction experienced by the solvent. The first class of systems consists of two single layers of graphene (Gr) separated by 3.804 nm, while the other has two four-layered silicon (Si) sheets oriented in the [111] direction and separated by 3.49 nm. A channel separation width is defined as the distance between the innermost layers of the top and bottom walls. For each wall, only the innermost layer in contact with the fluid is charged, with a wall charge value of $q_w = -(N_+ - N_-)e/N_w$, where N_+ is the number of cation particles, N_- is the number of anion particles, and N_w is the number of innermost wall particles. The slit systems are periodic in the x and y directions. In the z direction, a vacuum layer of size five times of the channel width separates the periodic images to exclude their interactions. Out of the six cases considered, four consist only of single ions (cation or anion) solvated in the confined water. In these cases, the charge neutrality is not achieved in the center region of the channel, leading to a large EDL and consequently high Debye lengths. In addition to pure counter-ion cases, we also consider the presence of co-ions in the confined water to understand the EOF in small Debye length situations. Subsequently, confined MD (both equilibrium and non-equilibrium) simulations are performed to compute the relevant quantities as a benchmark. For all of the MD simulations involving multiple ions in water, long range electrostatic interactions are considered via Particle-Particle Particle-Mesh (PPPM) method to ensure accuracy in computed forces. The temperature of the fluid (both ion and solvent) is set at 300 K using the Nosé-Hoover thermostat⁵⁵ with a time constant of 0.2 ps. In the NEMD simulations, the thermostat is not coupled to the streaming direction to avoid any artifacts in the simulation. The equations of motion are integrated using the velocity-Verlet algorithm with a time step of 1 fs. Table II provides the values of wall

TABLE II. Summary of the systems considered in the present study.

System	Wall type	Wall charge density (C/m^2)	E_x^{ext} (V/nm)	ζ_0 ((kJ-ps/mol)/ nm^2)
Na-Gr	Graphene	-0.1527	+0.015	7.95×10^2
Cl-Gr	Graphene	+0.1527	-0.02	1.131×10^3
NaCl-Gr	Graphene	-0.1018	+0.015	5.13×10^2
Na-Si	Silicon	-0.1242	+0.25	6.293×10^4
Cl-Si	Silicon	+0.1242	-0.15	4.692×10^5
NaCl-Si	Silicon	-0.0621	+0.2	3.872×10^4

charge density, the applied electric field to generate EOF, along with the nomenclature of the cases under consideration for brevity.

For EMD simulations, systems are equilibrated for 5 ns. After that, a production run of 10 ns is performed. Data are stored at every 5 fs for the computation of VACF in the bulk EMD simulations, and every 20 fs in confined EMD cases for computing the relevant time correlations in Eq. (18). For NEMD simulations, the EOF is allowed to develop for 10 ns, and subsequently, a production run is performed for 15 ns to obtain the fully developed, steady state velocity profiles, with data stored at every 0.1 ps. The macroscopic quantities from each case are ensemble averaged over 10 statistically identical MD simulations, which differ by the initial configuration of particles and the seed of the Maxwellian velocity distribution.

In the transport model, the slip plane location (δ) is defined using the tolerance on the solvent density as 10^{-3} molecules/ nm^3 , and it is approximately one solvent molecular diameter ($1\sigma_0$) away from the wall. To compute the species interfacial friction, 2D GLE simulations are performed with a time step of 0.01 ps. About 5×10^4 instances of particle trajectories of 500 ps are generated to compute the relevant time correlations. Data are saved at every other step (0.02 ps) and the first 100 ps is discarded to allow for equilibration. The numerical method for the time integration of the GLE is outlined elsewhere.⁴⁷

As a metric of speedup, we compare the Central Processing Unit (CPU) time, which is real wall-clock time multiplied

by the number of parallel processors in a simulation. A representative GLE simulation for 100 independent particles (single processor task) for 100 ps equilibration and 400 ps production run takes about 20 s of CPU time. Such small computation time permits us to perform GLE calculations on a personal workstation in contrast to MD simulations, which require massive parallelization. The continuum formulation typically takes 5 s, where meaningful data for velocity profiles from NEMD simulation require 11 520 CPU hours of production runs.

VI. RESULTS

In this section, we compare the accuracy of the proposed multiscale transport model for EOF by comparing its predicted velocity profiles against the NEMD simulation results. We first elucidate the limitations of the classical model for the 1D EOF that uses the mean-field Gouy-Chapman model for the ion concentration profiles, in conjunction with a constant viscosity based 1D Stokes equation with no-slip boundary conditions for the solvent velocity profile. In the classical model, the Neumann boundary condition of the wall charge density is applied at the slip plane. The classical EOF model is different from the multiscale transport model in several aspects. First, since it assumes a mean-field distribution of ions, it leads to a different measure of the driving force on the solvent (see second term in Eq. (1)). Second, due to the assumption of a constant value of the solvent viscosity, the effects of viscosity enhancement due to the interfacial layering of the solvent and ions are not captured. Finally, the effects of interfacial slip are also absent in the classical model. The limitations of the classical model in predicting the velocity profile of a nanoscale EOF can be understood from Figs. 2(a) and 2(b), where we compare its results with the NEMD calculations for the NaCl-Si case. It can be clearly observed that although the general features of the nanoscale EOF are resolved using the classical model, it lacks the quantitative accuracy, as it does not account for the aforementioned attributes.

The proposed multiscale transport model seeks to correct the deficiencies of a classical EOF model. Here, we first

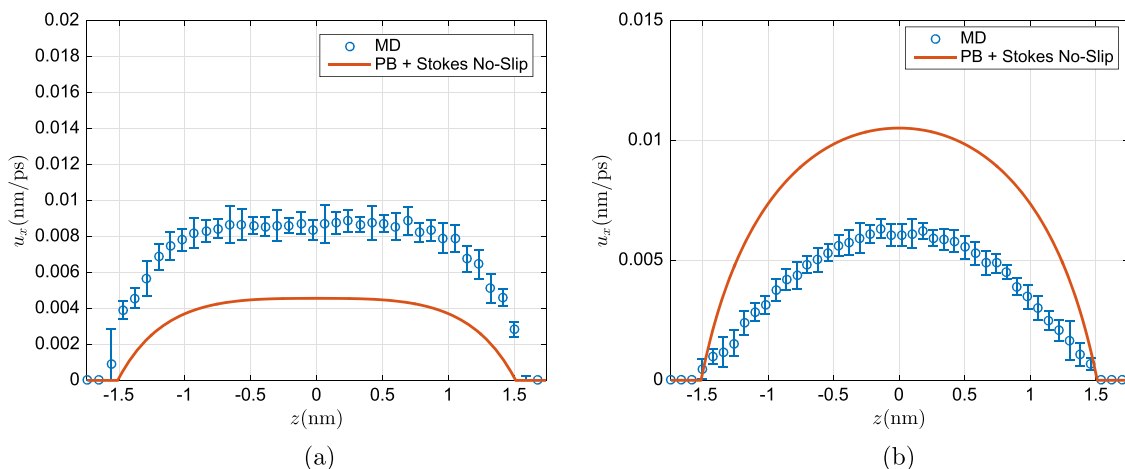


FIG. 2. Classical model predictions (using $\mu(z) = 0.65$ cP) of EOF velocity profiles for (a) NaCl-Si and (b) Cl-Si systems. Classical results are in solid line (red), while MD results are represented by error bars (blue).

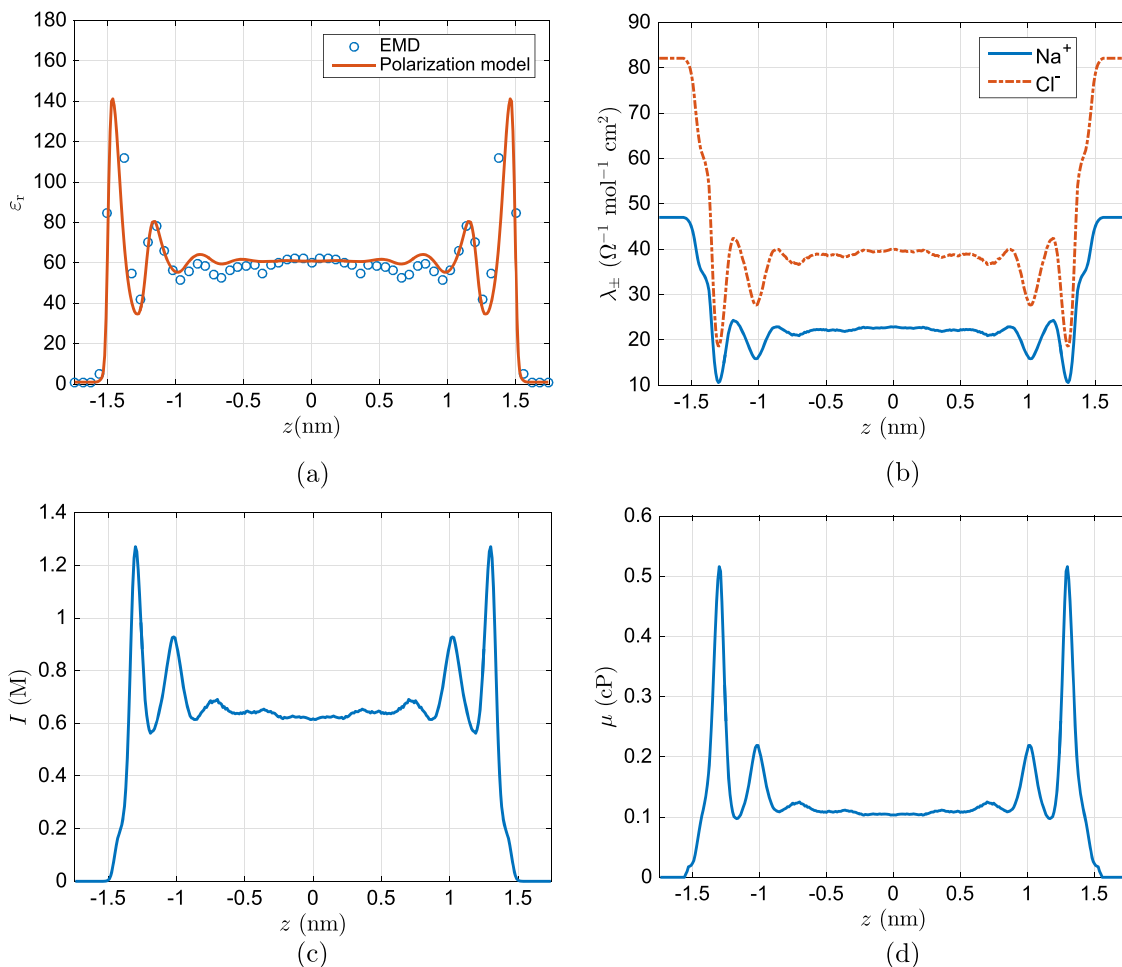


FIG. 3. (a) Relative permittivity from polarization model (red line, using $\epsilon_{r,b} = 60$ and $\mu_d = 4.18$ D) and its comparison with EMD computed values (blue circles), (b) ionic conductivities, (c) ionic strength, and (d) excess viscosity for the NaCl–Si system.

estimate the viscosity variation in the nanochannel. To compute the viscosity profile, we calculate the relative dielectric permittivity profile $\epsilon_r(z)$ of SPC/E water using the polarization model (Eq. (10)). We plot the resultant permittivity profile for the NaCl–Si system in Fig. 3(a) and compare it with the EMD value computed using the method illustrated in Ref. 56. A reasonable agreement between the two profiles is observed, and therefore the polarization model is subsequently used to estimate the variation of the relative permittivity in all the cases considered. Next, we estimate the inhomogeneity in the ionic conductivity. To this end, we first calculate the limiting value of the ion diffusion using ion VACF obtained from bulk ion EMD simulations described in Sec. V as

$$D_{\pm}^0 = \frac{1}{3} \int_0^{\infty} \langle v_{\pm}(0) \cdot v_{\pm}(t) \rangle dt, \quad (20)$$

where the vector value of ion velocity is used to calculate the VACF as it is isotropic in a bulk system. We obtain the values $D_+^0 = 1.26 \times 10^{-3}$ nm²/ps and $D_-^0 = 2.28 \times 10^{-3}$ nm²/ps. The resultant ionic conductivity profiles of Na⁺ and Cl⁻ ions computed using Eqs. (16) and (17) for the NaCl–Si system are plotted in Fig. 3(b). It can be understood from the plot that the ionic conductivities in the interfacial region show oscillations due to the interfacial layering of the

ions, and the location of their minimum value is consistent with the location of the peaks of the ionic strength profile (Fig. 3(c)). The phenomenon of interfacial solvent thickening can be understood from Eq. (8) that displays an inverse relationship between the ionic conductivities and solvent viscosity. As the ion mobility in the interfacial region is significantly hindered, the resultant interfacial viscosity of the surrounding solvent is increased.^{18,23} To observe this, we also plot the variation of the excess part of the viscosity due to the electrostatic effects $\mu_{ex}(z)$ for the NaCl–Si system in Fig. 3(d) where it can be seen that it closely resembles the ionic strength profile.

We now compare the friction coefficient defined in Eq. (18) and the intermediate time correlations obtained using GLE versus EMD calculations. We consider the contributions from the representative solvent particles in the small interfacial region,^{26,57} which is defined as the region spanned from the wall up to a cutoff distance of $1\sigma_0$ normal to the wall. We use the initial time occupancy based method to compute the time correlations, where all particles present in the interfacial region at the initial time are considered in the computation of total friction, regardless of their final location.⁵⁸ We present the FACF for Na–Gr (Fig. 4(a)), Cl–Gr (Fig. 4(b)), and NaCl–Gr (Fig. 4(c)) systems, where a good comparison between the GLE and EMD computed correlations is observed. It can also

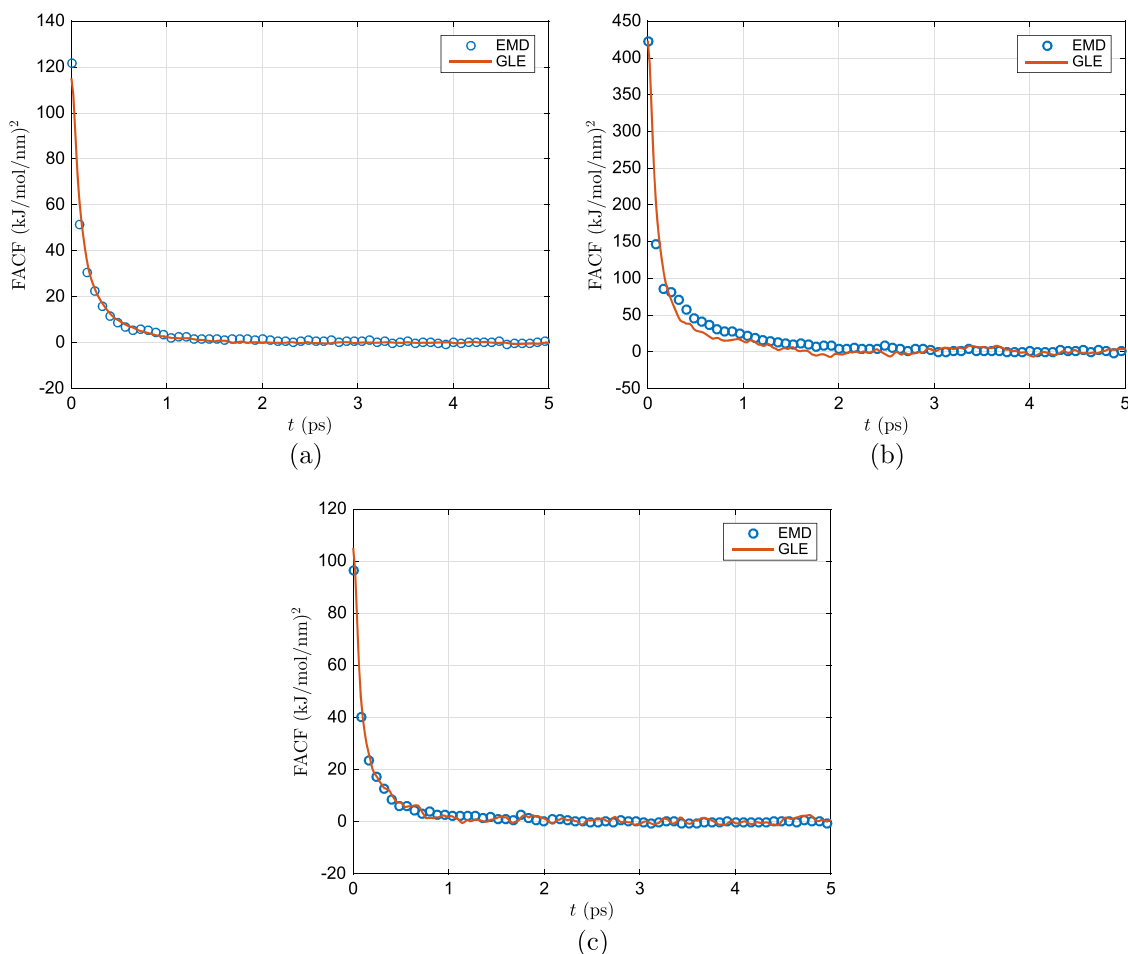


FIG. 4. Wall-solvent FACS from GLE (bold line, red) and EMD (circles, blue) for (a) Na-Gr, (b) Cl-Gr, and (c) NaCl-Gr systems.

be inferred from the plots that the variance of FACF is higher for the positively charged wall system (Cl-Gr), as compared to the negatively charged wall systems (Na-Gr and NaCl-Gr). Also, the relaxation time of the FACF in the Cl-Gr system is slightly higher than the other two cases. Due to the preferred orientation of the SPC/E water near a positively charged surface, the oxygen atom in the water molecule is closer to the wall compared to hydrogen atoms, leading to a higher value

of attractive LJ forces. Similar observations have been presented in Ref. 21, where they have split the contributions of the FACF into LJ-LJ, LJ-ES, and ES-ES, where ES stands for electrostatic contributions. Further, they have argued that the contributions from the LJ-ES term are significantly higher than those of ES-ES. Therefore, the orientational effects contribute significantly to the variance of FACF. A slight increase in the relaxation time also indicates that the water molecule

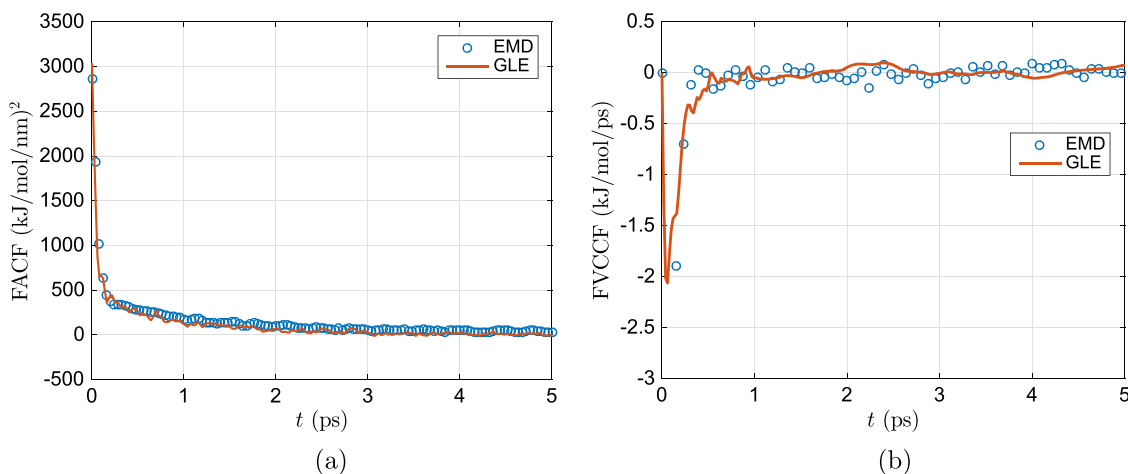


FIG. 5. Wall-solvent (a) FACF and (b) FVCCF calculated using GLE (bold line, red) and EMD (circles, blue) for NaCl-Si system.

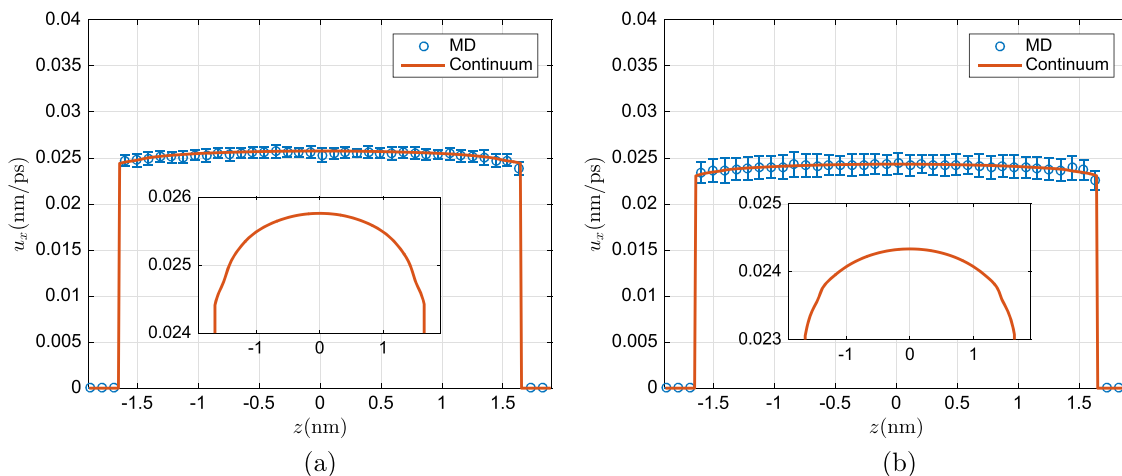


FIG. 6. EOF velocity profiles for (a) Na-Gr and (b) Cl-Gr systems. Continuum results are in solid line (red), while MD results are represented by error bars (blue). Insets show the viscous contributions from the multiscale transport model to the EOF in more detail. Model parameters are presented in Table II.

stays close to the positively charged wall a little longer before being re-thermalized. A similar pattern is also observed in the silicon wall cases. Also, for silicon walls, the increased value of LJ energy parameter of wall-solvent pair potential along with its lattice structure gives rise to a significantly higher force variance (Fig. 5(a)) than those observed for graphene systems. In addition to that, a significant coupling between the wall-solvent force and velocity is present as depicted by a non-zero value of the FVCCF (Fig. 5(b)). This phenomenon is not uniquely associated with the presence of wall charges and has been observed for a pure water case,²⁴ where both the FVCCF and FVCCF contribute to the interfacial friction in the case of silicon wall, compared to the graphene wall where the FVCCF is negligible. The values of the friction coefficient for different cases are reported in Table II, where the friction parameter is higher for a silicon wall as compared to graphene. Also, for a similar magnitude of wall charges, its value is systematically higher for positively charged walls (compare Na-Gr with Cl-Gr and their respective silicon counterparts). Additionally, increasing the wall charge density also increases the friction coefficient.

Next, we discuss the EOF velocity profiles obtained from the multiscale transport model and compare them with NEMD profiles. The EOF velocity profiles for Na-Gr and Cl-Gr cases are plotted in Figs. 6(a) and 6(b). These exhibit plug type flow and are in contrast with the EOF profiles obtained for Na-Si (Fig. 7(a)) and Cl-Si (Fig. 7(b)), where viscous contributions to the flow are apparent. This is because the friction parameter for graphene walls is almost two orders of magnitude smaller than that for silicon walls. The lattice structure of the graphene wall and the low wall-solvent LJ energy parameter collectively provide a smooth landscape for solvent particles. Although accounted for in the transport model, the viscous features of the EOF are obscured for graphene systems due to a high degree of hydrodynamic slip (see insets in Figs. 6(a) and 6(b)). Among the silicon systems, the viscous effects are more pronounced in the Cl-Si case compared to those in Na-Si, which is consistent with the previous observations.¹⁸ Since the charge neutrality is not achieved in the region far away from the wall (specifically due to the absence of co-ions), the shear stress is non-zero except at the center of the channel from symmetry considerations. This results in a non-zero

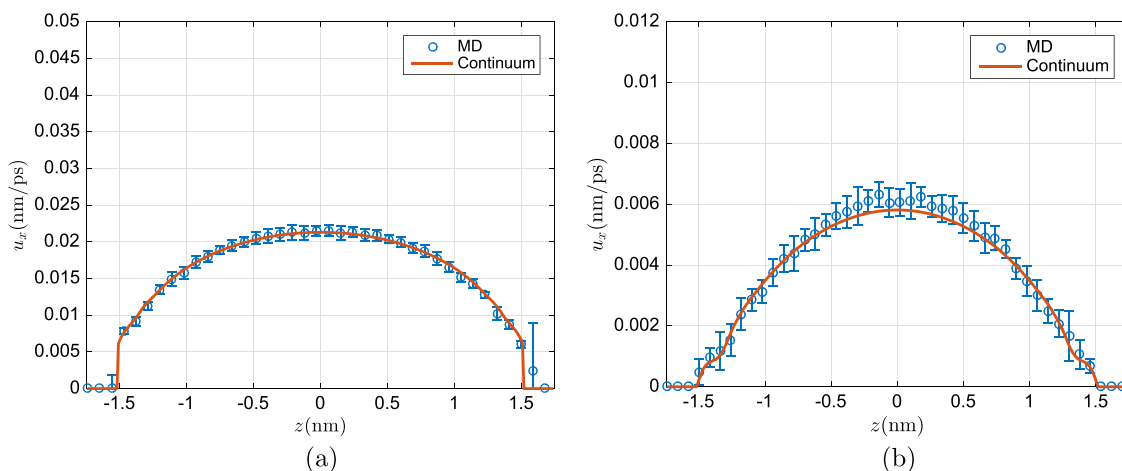


FIG. 7. EOF velocity profiles for (a) Na-Si and (b) Cl-Si systems. Continuum results are in solid line (red), while MD results are represented by error bars (blue). Model parameters are presented in Table II.

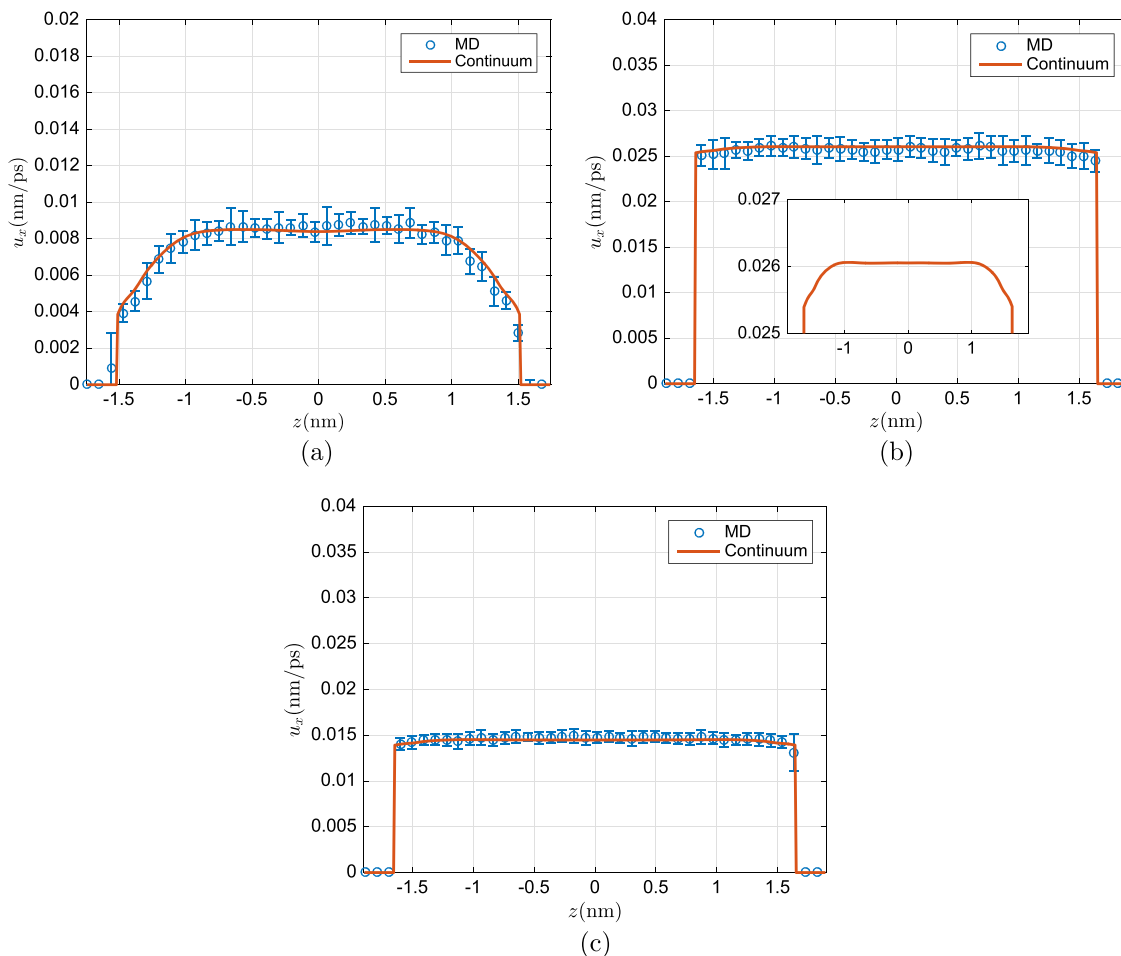


FIG. 8. EOF velocity profiles for (a) NaCl-Si, (b) NaCl-Gr, and (c) NaCl-Gr using the force-field of carbon-water from the work of Wu and Aluru.⁵⁹ Continuum results are in solid line (red), while MD results are represented by error bars (blue). Inset in (b) shows the viscous contributions from multiscale transport model to the EOF in more detail. Model parameters are presented in Table II.

strain rate, resulting in a viscosity mediated parabolic velocity profile.

For the NaCl-Si case (Fig. 8(a)), because of high interfacial friction (less slip) and charge neutrality in the bulk like region of the channel, a conventional form of the EOF profile is observed where velocity gradients are pronounced in the EDL region along with a plug-like behavior in the center region of the channel. The NaCl-Gr system, owing to a large slip contribution, again exhibits a slip dominant profile as understood from Fig. 8(b). However, closer inspection of the velocity profile shown in the inset displays similar viscous features as the NaCl-Si system. We also studied the NaCl-Gr case with the water-graphene force-field provided by Wu and Aluru,⁵⁹ for an identical driving electric field ($E_x^{\text{ext}} = +0.015$ V/nm) in Fig. 8(c). The parameters of this force field are developed from the *ab initio* calculations and predict the graphite-water contact angle in close agreement with experimental results. It is observed that the slip velocity decreases due to the hydrophilic nature of the graphene wall resulting in a higher value of interfacial friction ($\zeta_0 = 9.361 \times 10^2$ kJ-ps/mol/nm²). Based on these observations, one can conclude that the wall-solvent interaction parameters affect the flow profile in a significant manner, and our EOF model is able to capture these effects accurately.

VII. CONCLUSIONS

We have presented an interfacial friction based multiscale transport model for electroosmotic flow. Spatial inhomogeneity in the solvent viscosity is modeled with separate contributions due to the layering of solvent density and ion densities. Local viscosity variations include contributions from the solvent structure using LADM and ion concentration dependent excess contributions using the Onsager-Fuoss expression. The interfacial friction dependent slip velocity is used as the boundary condition. The friction parameter links the field based continuum description of the EOF to the atomistic one via the wall-solvent FACF and FVCCF. These time correlations are computed using a refined GLE framework that uses the electrochemical wall-solvent force map as an input and is observed to compare well with their EMD computed values. The segregation of flow profile into the slip and viscous contributions allows us to separately predict the phenomenon of interfacial thickening of the solvent and enhanced interfacial friction due to the coupling of LJ and electrostatic forces. It is inferred that the interfacial friction for a positively charged wall is higher compared to that for the negatively charged wall of equal charge density magnitude. The proposed model shows a good agreement between the EOF velocity profiles and

the NEMD computed ones for a variety of input parameters such as wall-type, surface charge densities, and applied electric fields.

ACKNOWLEDGMENTS

This work was supported by AFOSR (Grant No. FA9550-12-1-0464) and NSF (Grant Nos. 1264282, 1420882, 1506619, and 1545907). R.B. thanks Sikandar Mashayak for helpful discussions on the polarization model. The authors acknowledge the use of the Taub cluster provided by the Computational Science and Engineering Program at the University of Illinois.

- ¹V. Marry, J.-F. Dufrêche, M. Jardat, and P. Turq, *Mol. Phys.* **101**, 3111 (2003).
- ²J.-F. Dufrêche, V. Marry, N. Malikova, and P. Turq, *J. Mol. Liq.* **118**, 145 (2005).
- ³S. Y. Noskov, W. Im, and B. Roux, *Biophys. J.* **87**, 2299 (2004).
- ⁴C. R. Buie, J. D. Posner, T. Fabian, S.-W. Cha, D. Kim, F. B. Prinz, J. K. Eaton, and J. G. Santiago, *J. Power Sources* **161**, 191 (2006).
- ⁵Y. Ren and D. Stein, *Nanotechnology* **19**, 195707 (2008).
- ⁶W. Sparreboom, A. van den Berg, and J. C. T. Eijkel, *Nat. Nanotechnol.* **4**, 713 (2009).
- ⁷J. Feng, M. Graf, K. Liu, D. Ovchinnikov, D. Dumcenco, M. Heiranian, V. Nandigana, N. R. Aluru, A. Kis, and A. Radenovic, *Nature* **536**, 197 (2016).
- ⁸M. Heiranian, A. B. Farimani, and N. R. Aluru, *Nat. Commun.* **6**, 8616 (2015).
- ⁹G. E. Karniadakis, A. Beskok, and N. R. Aluru, *Microflows and Nanoflows: Fundamentals and Simulation* (Springer, 2005).
- ¹⁰B. J. Kirby, *Micro- and Nanoscale Fluid Mechanics: Transport in Microfluidic Devices* (Cambridge University Press, 2010).
- ¹¹O. Stern, *Z. Elektrochem.* **30**, 508 (1924).
- ¹²R. Qiao and N. R. Aluru, *J. Chem. Phys.* **118**, 4692 (2003).
- ¹³J. Bikerman, *London, Edinburgh Dublin Philos. Mag. J. Sci.* **33**, 384 (1942).
- ¹⁴E. Gongadze, U. van Rienen, V. Kralj-Iglič, and A. Iglič, *Comput. Methods Biomech. Biomed. Eng.* **16**, 463 (2013).
- ¹⁵R. Hartkamp, B. Siboulet, J.-F. Dufrêche, and B. Coasne, *Phys. Chem. Chem. Phys.* **17**, 24683 (2015).
- ¹⁶D. M. Huang, C. Cottin-Bizonne, C. Ybert, and L. Bocquet, *Langmuir* **24**, 1442 (2008).
- ¹⁷J. Lyklema and J. Overbeek, *J. Colloid Sci.* **16**, 501 (1961).
- ¹⁸R. Qiao and N. R. Aluru, *Appl. Phys. Lett.* **86**, 143105 (2005).
- ¹⁹R. Qiao and N. R. Aluru, *Colloids Surf., A* **267**, 103 (2005).
- ²⁰R. Qiao and N. R. Aluru, *Langmuir* **21**, 8972 (2005).
- ²¹L. Joly, C. Ybert, E. Trizac, and L. Bocquet, *J. Chem. Phys.* **125**, 204716 (2006).
- ²²R. Netz, *Phys. Rev. Lett.* **91**, 138101 (2003).
- ²³P. Wu and R. Qiao, *Phys. Fluids* **23**, 072005 (2011).
- ²⁴R. Bhadauria, T. Sanghi, and N. R. Aluru, *J. Chem. Phys.* **143**, 174702 (2015).
- ²⁵R. Bhadauria and N. R. Aluru, *J. Chem. Phys.* **145**, 074115 (2016).
- ²⁶K. Huang and I. Szlufarska, *Phys. Rev. E* **89**, 032119 (2014).
- ²⁷L. Onsager and R. M. Fuoss, *J. Phys. Chem.* **36**, 2689 (1931).
- ²⁸I. Bitsanis, J. J. Magda, M. Tirrell, and H. T. Davis, *J. Chem. Phys.* **87**, 1733 (1987).
- ²⁹I. Bitsanis, T. K. Vanderlick, M. Tirrell, and H. T. Davis, *J. Chem. Phys.* **89**, 3152 (1988).
- ³⁰T. K. Vanderlick, L. E. Scriven, and H. T. Davis, *J. Chem. Phys.* **90**, 2422 (1989).
- ³¹A. V. Raghunathan, J. H. Park, and N. R. Aluru, *J. Chem. Phys.* **127**, 174701 (2007).
- ³²T. Sanghi and N. R. Aluru, *J. Chem. Phys.* **132**, 044703 (2010).
- ³³T. Sanghi and N. R. Aluru, *J. Chem. Phys.* **136**, 024102 (2012).
- ³⁴S. Y. Mashayak and N. R. Aluru, *J. Chem. Theory Comput.* **8**, 1828 (2012).
- ³⁵S. Y. Mashayak and N. R. Aluru, *J. Chem. Phys.* **137**, 214707 (2012).
- ³⁶S. Y. Mashayak, M. H. Motevaselian, and N. R. Aluru, *J. Chem. Phys.* **142**, 244116 (2015).
- ³⁷M. H. Motevaselian, S. Y. Mashayak, and N. R. Aluru, *J. Chem. Phys.* **143**, 124106 (2015).
- ³⁸S. Mashayak and N. Aluru, *J. Chem. Phys.* **146**, 044108 (2017).
- ³⁹H. Falkenhagen, *Phys. Z* **32**, 745 (1931).
- ⁴⁰A. Chandra and B. Bagchi, *J. Chem. Phys.* **113**, 3226 (2000).
- ⁴¹E. Gongadze, A. Velikonja, Š. Perutkova, P. Kramar, A. Maček-Lebar, V. Kralj-Iglič, and A. Iglič, *Electrochim. Acta* **126**, 42 (2014).
- ⁴²M. R. Wright, *An Introduction to Aqueous Electrolyte Solutions* (John Wiley & Sons, Inc., 2007), pp. 245–380.
- ⁴³C. A. J. Appelo, Specific conductance—How to calculate, to use, and the pitfalls; <http://www.hydrochemistry.eu/exmpls/sc.html>.
- ⁴⁴H. Mori, *Prog. Theor. Phys.* **33**, 423 (1965).
- ⁴⁵R. Zwanzig, *Nonequilibrium Statistical Mechanics* (Oxford University Press, 2001).
- ⁴⁶H. Grabert, *Projection Operator Techniques in Nonequilibrium Statistical Mechanics* (Springer, Berlin, 1982).
- ⁴⁷T. Sanghi and N. R. Aluru, *J. Chem. Phys.* **141**, 174707 (2014).
- ⁴⁸S. Plimpton, *J. Comput. Phys.* **117**, 1 (1995).
- ⁴⁹H. J. C. Berendsen, J. R. Grigera, and T. P. Straatsma, *J. Phys. Chem.* **91**, 6269 (1987).
- ⁵⁰D. E. Smith and L. X. Dang, *J. Chem. Phys.* **100**, 3757 (1994).
- ⁵¹G. A. Orozco, O. A. Moulton, H. Jiang, I. G. Economou, and A. Z. Panagiotopoulos, *J. Chem. Phys.* **141**, 234507 (2014).
- ⁵²M. Gordillo and J. Marti, *Chem. Phys. Lett.* **329**, 341 (2000).
- ⁵³S. H. Lee and J. C. Rasaiah, *J. Phys. Chem.* **100**, 1420 (1996).
- ⁵⁴S. Koneshan and J. C. Rasaiah, *J. Chem. Phys.* **113**, 8125 (2000).
- ⁵⁵S. Nosé, *J. Chem. Phys.* **81**, 511 (1984).
- ⁵⁶D. J. Bonthuis, S. Geckle, and R. R. Netz, *Phys. Rev. Lett.* **107**, 166102 (2011).
- ⁵⁷J. S. Hansen, B. D. Todd, and P. J. Daivis, *Phys. Rev. E* **84**, 016313 (2011).
- ⁵⁸E. R. Pinnick, S. Erramilli, and F. Wang, *Mol. Phys.* **108**, 2027 (2010).
- ⁵⁹Y. Wu and N. R. Aluru, *J. Phys. Chem. B* **117**, 8802 (2013).